nanomaterials

MDPI

Article

Flame Spray Pyrolysis Synthesis of Vo-Rich Nano-$SrTiO_{3-x}$

Areti Zindrou, Pavlos Psathas and Yiannis Deligiannakis *

Laboratory of Physical Chemistry of Materials & Environment, Department of Physics, University of Ioannina, 45110 Ioannina, Greece; a.zindrou@uoi.gr (A.Z.); pavlospsatha@gmail.com (P.P.)
* Correspondence: ideligia@uoi.gr; Tel.: +30-2651008662

Abstract: Engineering of oxygen vacancies (Vo) in nanomaterials allows diligent control of their physicochemical properties. $SrTiO_3$ possesses the typical ABO_3 structure and has attracted considerable attention among the titanates due to its chemical stability and its high conduction band energy. This has resulted in its extensive use in photocatalytic energy-related processes, among others. Herein, we introduce the use of Flame Spray Pyrolysis (FSP); an industrial and scalable process to produce Vo-rich $SrTiO_3$ perovskites. We present two types of Anoxic Flame Spray Pyrolysis (A-FSP) technologies using CH_4 gas as a reducing source: Radial A-FSP (RA-FSP); and Axial A-FSP (AA-FSP). These are used for the control engineering of oxygen vacancies in the $SrTiO_{3-x}$ nanolattice. Based on X-ray photoelectron spectroscopy, Raman and thermogravimetry-differential thermal analysis, we discuss the role and the amount of the Vos in the so-produced nano-$SrTiO_{3-x}$, correlating the properties of the nanolattice and energy-band structure of the $SrTiO_{3-x}$. The present work further corroborates the versatility of FSP as a synthetic process and the potential future application of this process to engineer photocatalysts with oxygen vacancies in quantities that can be measured in kilograms.

Keywords: $SrTiO_3$; strontium titanate; perovskite; flame spay pyrolysis; oxygen vacancies; Vo; lattice defects; photocatalyst

Citation: Zindrou, A.; Psathas, P.; Deligiannakis, Y. Flame Spray Pyrolysis Synthesis of Vo-Rich Nano-$SrTiO_{3-x}$. *Nanomaterials* **2024**, *14*, 346. https://doi.org/10.3390/nano14040346

Academic Editors: Antonio Guerrero-Ruiz and Nikolaos Dimitratos

Received: 20 December 2023
Revised: 7 February 2024
Accepted: 8 February 2024
Published: 11 February 2024

1. Introduction

Perovskite-oxides with the classical ABO_3 structure have attracted considerable attention for their functional properties, e.g., their multiferroic properties [1,2]. They are used in the electronics industry [3], in enhanced power conversion efficiencies [4]; and they are also used extensively as photocatalysts due to their structural, compositional and stoichiometric flexibility [5]. Among the titanates, much attention has been paid to strontium titanate ($SrTiO_3$), a perovskite with a cubic structure [6] that possesses several advantageous features, including low cost [7], chemical stability and thermal resilience (melting point reaching 2080 °C); carbon and sulfur tolerance further contributes to the structural stability [8]. Its highly-reducing conduction-band-edge energy position (E_{CB}) at −1.2 eV vs. NHE (Normal Hydrogen Electrode) [9,10] renders $SrTiO_3$ as a promising platform for H_2-production or CO_2-reduction photocatalytic systems. However, $SrTiO_3$ is characterized by a drawback; namely, a wide 3.2 eV band gap, restricting absorption to ultraviolet (UV) photons [11]. To overcome this constraint, a variety of strategies are implemented. For instance, structural defect engineering (metal or oxygen vacancies), element doping and co-catalyst heterostructures have been implemented, with great results [12].

$SrTiO_3$ has demonstrated high optimizability for specific technologies through crystal lattice engineering, enabling the control of structural, optical, and electronic properties to enhance photocatalytic efficiency [13,14]. In this context, oxygen vacancies (Vo) exert a remarkably influential role in various optoelectronic properties [12].

Vo-engineering allows fine-tuning of various properties; e.g., surface Vos can act as photogenerated-species' traps, facilitating the transfer to adsorbed compounds and consequently averting {electron-hole, e^-/h^+} recombination. In contrast, typically, bulk

Vos can merely function as $\{e^-\}$ traps, facilitating the recombination of photogenerated $\{e^-/h^+\}$; i.e., diminishing photocatalytic performance [15]. Recently, we have exemplified this for the case of Vo-rich ZrO_{2-x} [16] where diligent control of the amount and location of Vo was the key parameter for enhancing its photocatalytic H_2-production.

Numerous efforts have been reported in the literature regarding the introduction of oxygen vacancies in the $SrTiO_3$ lattice. Recently, Li et al. have reported that the formation of oxygen vacancies in $SrTiO_3$ nanofibers through calcination in an H_2/N_2 atmosphere can significantly improve photocatalytic H_2 production by facilitating charge transfer and slowing down their recombination without the use of a cocatalyst [17]. Similar results have been reported by Fan et al.; heating of pristine $SrTiO_3$ under a carbon-containing reducing atmosphere yielded a distorted surface layer with oxygen vacancies [18]. These vacancies can provide suitable energy levels for visible light activity and improve charge separation. In another work, Qin et al. have demonstrated that the reduction of oxygen vacancies in $SrTiO_3$ by introducing La^{3+} and Al^{3+} qualifies as an effective strategy to boost photocatalytic H_2 and O_2 evolution [19]. Doping with Al^{3+} introduces the oxygen vacancies into the perovskite, resulting in a conversion of Ti^{3+} to Ti^{4+}. At the same time, La^{3+} doping balances the effect of Al^{3+}, reversing the transformation trend of the semiconductor. However, a common problem among various synthetic approaches is the milligram-scale quantities they yield and the size of the produced nanoparticles, which exceeds 200 nm.

In this context, flame spray pyrolysis (FSP) is a versatile technology for the engineering of multifunctional nanostructures and nanodevices [20] with controllable characteristics (size, phase, crystallinity), and can provide nanoparticles at large quantities. Recently, we have demonstrated that FSP can be successfully employed to synthesize highly-photoactive perovskite materials, e.g., $BiFeO_3$ [21], $NaTaO_3$ [22]. Herein, we show that FSP-made $SrTiO_3$ with controlled Vos is a novel approach towards enhanced photoactivity. Previously, Yuan et al. presented FSP-made $SrTiO_3$ with dopings of Co, Fe, Mn, Ni and Cu [23,24]. Our previous work showcased La-doping and CuO-heterojunction on $SrTiO_3$ enhancement and selective H_2 vs. CH_4 photocatalytic production from H_2O/CH_3OH [25].

Herein, the specific aims of the present works were: (i) to develop FSP protocols for controlled Vo-engineering in nanosized $SrTiO_{3-x}$, employing an advanced FSP approach in which the combustion stoichiometry was controlled by the FSP-design and operating conditions [16,20,26,27]; (ii) to study the structural and spectroscopic properties of the so-produced $SrTiO_{3-x}$; (iii) to extend and highlight the versatility of A-FSP as a technique capable of producing large quantities of elaborated nanostructures.

2. Materials and Methods

2.1. Synthesis of Reduced $SrTiO_{3-x}$ by Anoxic Flame Spray Pyrolysis (A-FSP)

A library of four $SrTiO_{3-x}$ (for convenience, these are codenamed STO) perovskites was prepared in an enclosed single-nozzle FSP reactor using two different Anoxic-FSP configurations (see Figure 1A,B). The A-FSP reactor set-up uses CH_4 to control the anoxic-combustion environments, as exemplified in our recent works [16,26,27]. This CH_4 is additional to the classically used CH_4 in the pilot-flame of FSP [28]. The two A-FSP configurations in Figure 1A,B are codenamed Radial- and Axial-A-FSP; these define the way in which CH_4 is introduced, respectively. In all cases, the FSP-nozzle was enclosed by a cylindrical metal chamber consisting of two concentric tubes, a sinter metal tube (outer tube) and a perforated metal tube (inner tube) to isolate the flame from the surrounding atmosphere, as has been described in detail in previous works [16,26,27,29]. The so-produced materials (listed in Table 1) are codenamed STO-R and STO-A for Radial- and Axial-A-FSP, respectively.

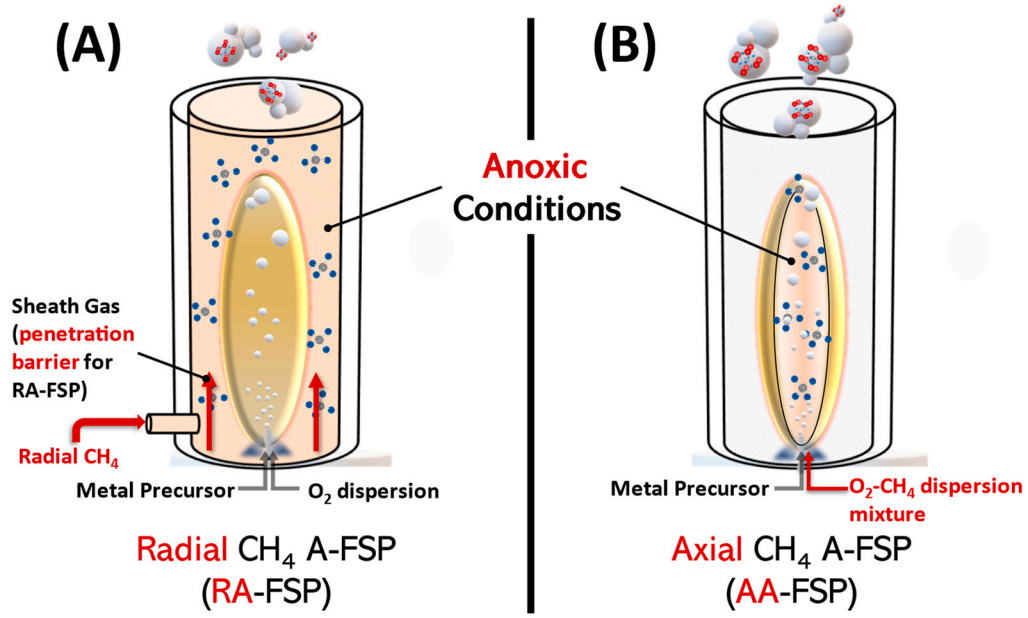

Figure 1. (**A**) Schematic representation of Radial-CH_4 and (**B**) Axial-CH_4 A-FSP processes.

Table 1. A-FSP conditions for the synthesis of Vo-rich $SrTiO_{3-x}$ perovskites.

Nanomaterial	Sheath Gas (L min^{-1})	P/D	Axial CH_4 (L min^{-1})	Radial CH_4 (L min^{-1})
Pristine STO	O_2: 10	5/5	-	-
STO-R3	N_2: 5	»	-	3
STO-R5	N_2: 5	»	-	5
STO-A1	N_2: 10	»	1	-
STO-A2	N_2: 10	»	2	-

Precursor solution was prepared by dissolving 0.2M Strontium acetate (97%, STREM (Newburyport, MA, USA)) and 0.2M Titanium (VI) isopropoxide (97%, Sigma-Aldrich (Saint Louis, MO, USA)) in a 1:1 mixture of acetic acid and xylene for the synthesis of perovskite $SrTiO_3$. The solution was fed into the FSP burner through a capillary at a flow rate of P = 5 mL min^{-1} and atomized into fine droplets using a dispersion flow rate of D_{total} = 5 L min^{-1}. The resulting spray was ignited and sustained by a premixed oxygen/methane pilot flame (O_2 4 L min^{-1}, CH_4 2 L min^{-1}) to initiate combustion. Finally, the pressure drop was fixed at 1.5–2 bars and the produced particles were collected in a glass microfiber filter (Hahnemühle GF 6 257) with the aid of a vacuum pump (BUSCH V40) and collected by scraping.

2.1.1. Radial-CH_4 Anoxic Flame Spray Pyrolysis (RA-FSP)

This RA-FSP process is similar to conventional FSP regarding the particle formation steps. Its difference lies in the radially introduced CH_4 gas surrounding the flame (Figure 1A). In addition, a suitable low sheath gas (N_2) flow of 5 L min^{-1} is used to allow the radially introduced CH_4 to penetrate the sheath gas barrier and react with the flame and the particles. Note that the role of N_2-sheath is double, maintaining the anoxic atmosphere during particle synthesis and aiding in the particle collection; i.e., via upwards convection. The production protocol was set up so that the materials are consistent with each other, i.e., precursor molarity, the pilot flame, and the P/D ratio were constant; thus, their comparison was focused on the additional insertion of CH_4; see Table 1. The so-produced materials are listed in Table 1 and codenamed "STO-RX" where x = the radial CH_4-inflow in L min^{-1}.

2.1.2. Axial CH_4 Anoxic Flame Spray Pyrolysis (AA-FSP)

In AA-FSP, a mixture of oxygen (O_2)/methane (CH_4) is used as a dispersion gas to promote a reducing environment insitu inside the flame [16,26]. The high combustion enthalpy of methane, i.e., 50–55 MJ kg^{-1}, increases the combustion temperature, which subsequently minimizes the deposition of graphitized carbon. In contrast to Radial A-FSP, it is employed at the moment of particle crystallization; thus, there is a higher chance of creating deficient centers in the material. By keeping constant the pilot flame and the P/D ratio and adjusting the D_1 (O_2)/D_2 (CH_4), two materials were prepared—codenamed STO-A1 and STO-A2—where D_2 = 1 L min^{-1} and 2 L min^{-1}, respectively. Herein, an N_2 sheath gas flow of 10 L min^{-1} was also used to decrease the overall oxygen concentration during the synthesis.

2.2. Structural Characterization of Materials

Powder X-ray diffraction (pXRD) was employed to analyze the crystal phase and structural properties of the flame-synthesized strontium titanate (STO) nanomaterials. A Bruker D8 Advance diffractometer employing CuKa radiation with a wavelength (λ) of 1.5405 Å, was utilized for the characterization. The scanning parameters included a step size of 0.03°, a scanning rate of 2 s per step, and a 2-theta angle range spanning from 10° to 80°. The diffractometer operated at a current of 40 mA and a generator voltage of 40 kV. The average crystallite size of the FSP-made nanopowders was calculated using the Scherrer equation [30] (1).

$$d_{XRD} = \frac{K\lambda}{(FWHM) \times \cos\theta} \quad (1)$$

where d_{XRD} is the crystallite size in nanometers (nm), K is a shape constant (0.9 in our case), λ is the wavelength of CuKa radiation, FWHM is the full width at half-maximum of the XRD peaks and θ is the peak diffraction angle. Further analysis of the XRD data involves Rietveld refinement using Profex, a graphical user interface program, which can yield the lattice parameter α.

Transmission Electron Microscopy (TEM) was utilized to investigate the morphology of the materials. This examination was carried out using an FEI Titan 80–300 S/TEM microscope, operating at a 300 kV accelerating voltage and a 21.5 mrad beam convergence angle. Prior to measurement, each nanopowder was dispersed in ethanol and subjected to sonication in a bath sonicator. The resulting suspension was then deposited as a single droplet onto a copper TEM grid coated with a thin carbon layer. To eliminate potential organic contaminants, the samples underwent a 3-s treatment in argon plasma using a Fischione Instruments 1020 Plasma Cleaner.

Ultraviolet-Visible Diffuse-Reflectance (UV-Vis DRS) absorption spectra were recorded using a PerkinElmer (Lambda 35) spectrometer to ascertain the energy gap values. $BaSO_4$ powder served as the standard background. The spectra were obtained at room temperature within the 200–800 nm range, employing a scanning step of 1 nm. The Kubelka–Munk method was then applied to calculate the energy gap values (Eg) [31].

Brunauer–Emmett–Teller (BET) analysis was employed to measure the Specific Surface Area (SSA) and the pore size distribution of the nanomaterials. A Quantachrome NOVAtouch_LX2 instrument was used to record the N_2 adsorption–desorption isotherms at 77 K. Prior to measurement, at least 200 mg of the FSP-made nanopowder was degassed at 100 °C for 16 h. The SSA values were calculated using the absorption data points in the range of 0.1−0.3 relative pressure P/Po. Pore radius analysis was obtained by the Barett–Joyner–Halenda (BJH) method [32] in the range of 0.35–0.99 P/Po. Moreover, based on BET data we can calculate the average particle diameter (d_{BET}) in nanometers using the following equation:

$$d_{BET} = \frac{6000}{\left(SSA_{BET} \text{ in } \frac{m^2}{g}\right) \times \left(\rho \text{ in } \frac{g}{cm^3}\right)} \quad (2)$$

where ρ symbolizes the density; in the case of $SrTiO_3$ this is equal to 5.11 g cm^{-3}. However, there are limitations in this calculation, i.e., the particles must be spherical or quasi-spherical.

Raman spectra were recorded using a HORIBA-Xplora Plus spectrometer coupled with an Olympus BX41 microscope. As an excitation source, a 785 nm diode laser was used and with the aid of a microscope the beam was focused on the sample. Before each measurement, each powder material was gently pressed between two glass plates to form a pellet-like shape. Raman spectra were recorded in the range of 100–1700 cm^{-1} and the spectra resolution was approximately 1–1.5 cm^{-1}, performing 30 accumulations at fixed intensity, i.e., 50% of the total intensity of the laser.

X-ray photoelectron spectroscopy (XPS) was utilized to investigate the oxidation states of Sr, Ti and O atoms. This analysis was conducted with a SPECS spectrometer featuring a twin Al-Mg anode X-ray source and a multi-channel hemispherical sector electron analyzer (HSA-Phoibos 100, Mansfield, MA, USA). The XPS measurements utilized a monochromatized Mg Kα line at 1253.6 eV, an analyzer pass-energy of 15 eV, and a base pressure of 2–5 $\times$ 10^{-9} mbar. Binding energies were referenced to the energy of the C1s carbon peak at 284.5 eV. Peak deconvolution was carried out using mixed Gaussian–Lorentzian functions, employing WinSpec software developed at the Laboratoire Interdisciplinaire de Spectroscopie Electronique, University of Namur, Belgium.

Thermogravimetry-differential thermal analysis (TG-DTA) was conducted to determine the mass change (Δm) of the nanopowders using a Setaram Labsys Evo instrument using a heat rate of 2 °C min^{-1} from 20 to 700 °C and a flow of synthetic air gas of 20 mL min^{-1}.

3. Results

Figure 2A shows the XRD patterns of the as-prepared nanomaterials, where the diffraction peaks match the diffraction peaks of the cubic perovskite structure of $SrTiO_3$ (PDF #81-9665). However, a closer inspection of the XRD patterns reveals the presence of small peaks at 26.4°, 29.1°, 35.8°, 41.7°, 51.8° and 60.4° that do not match the known XRD patterns of TiO_2 and/or SrO. Therefore, we attribute these small peaks to the presence of minor impurities. Thus, the XRD data confirm that both RA-FSP and AA-FSP protocols produce highly crystallized $SrTiO_3$ nanoparticles. d_{XRD} values were calculated from the peak at 32.4°, which corresponds to (110) using the Scherrer formula [30] and range between 41–58 nm, listed in Table 2.

TEM images (Figure 2B,C) show the formation of quasi-spherical $SrTiO_3$ particles forming neck-sintered aggregates, which are typical for FSP-made particles. Analysis of the TEM images using ImageJ, an open-access program, reveals the existence of a size-distribution from 10 to 150 nm (see Figure 2B,C inset figures), with most of the particles being between 10 and 40 nm, with a mean size of d_{TEM} = 17 $\pm$ 0.5 nm and 19.7 $\pm$ 1.3 nm for STO-R5 and STO-A2, respectively. We underline that these size distributions are a result of at least 100 particles and were obtained from several TEM images. These results are in good agreement with the structural characterization results of FSP-made $SrTiO_3$ particles from our previous work [25]. Comparison of d_{XRD} and d_{TEM} reveals a well-known effect in which larger particles dominate the diffraction patterns, while the contribution of smaller particles is less visible. Thus, XRD tends to overestimate the average particle size, while TEM gives us better information regarding the morphology of the material.

The N_2 adsorption/desorption isotherms (see Figure S1A–E) show the characteristic type-III isotherm with a negligible pore volume. A careful examination of the SSA values, listed in Table 2, and comparison with the XRD results indicates that: (i) d_{XRD} shows a moderate increase as CH_4-flows become higher, i.e., STO-R5 or STO-A2; and (ii) d_{BET} dramatically increases in STO-A1, STO-A2 (Table 2), i.e., when the Axial-A-FSP set-up was used. This d_{BET} increase was less-prominent in the STO-R3, R5 particles. This increase in d_{BET} indicates a strong promotion of the particle-aggregation that occurs when CH_4 is introduced in the dispersion-gas flow, which decreases when we enclose the burner and introduce CH_4 to the FSP set-up. These trends can be understood as follows: in the FSP

process, high temperature residence time is a key characteristic of the flame synthesis, which determines particle growth [33]. In an enclosed FSP-flame, introduction of CH_4—either radially or axially—increases the combustion enthalpy, resulting in higher temperatures that drive the growth of particle size.

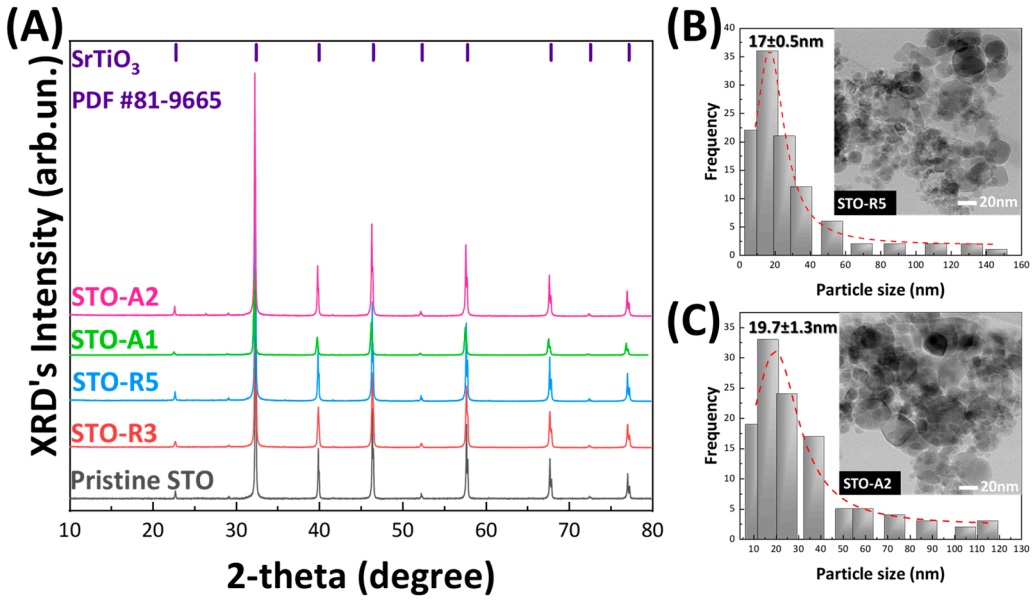

Figure 2. (**A**) XRD patterns of the pristine and reduced STO nanomaterials. (**B**,**C**) Size distribution graphs obtained from several TEM images for STO-R5 and STO-A2 materials. (*Inset Figures:* TEM image of STO-R5 and STO-A2).

Table 2. Structural characteristics of the reduced STO nanoparticles.

Nanomaterial	d_{XRD} (nm)	d_{BET} (nm)	SSA (m^2 g^{-1}) ($\pm$0.5)	Band Gap (E_g) (eV) ($\pm$0.05)
Pristine STO	45 $\pm$ 0.5	36 $\pm$ 0.5	32.3	3.17
STO-R3	41 $\pm$ 0.5	53 $\pm$ 0.5	22.2	3.23
STO-R5	58 $\pm$ 0.5	68 $\pm$ 0.5	17.4	3.22
STO-A1	43 $\pm$ 0.5	110 $\pm$ 0.5	10.7	3.19
STO-A2	54 $\pm$ 0.5	96 $\pm$ 0.5	12.2	3.27

The optical properties were measured using UV-Vis DRS spectroscopy. Pristine STO as a semiconductor possesses an indirect energy gap (E_g) of 3.25 eV and a direct energy gap of 3.75 eV. The bandgap values were estimated with a Tauc plot using the Kubelka–Munk method [31]; see Figure 3B. As shown in Figure 3A, all FSP-produced materials exhibit an absorption edge that begins at 390 nm, yielding an energy gap of 3.2 eV approximately. For convenience, the E_g-values of the materials are listed in Table 2. Although the E_g values seem not to be affected by much, i.e., E_g ~ 3.1–3.2 eV, a strong offset is observed in the UV-Vis DRS spectrum of all anoxic STO materials, with most prominent that for STO-R5 > STO-R3 > STO-A2 > STO-A1. This trend, together with minor shifts in the E_g values, is interpreted as being manifestations of the formation of Urbach-states [34]. In brief, Urbach-states appear as band-tails at the edges of the conduction- and valence-band in semiconductors, and can typically be created in partially reduced oxides [35]. Due to their quasi-symmetric distribution, these band-tails do not manifest themselves in clear-change in the band-gap, but they rather cause characteristic distribution of the UV-Vis absorbance extending over a wide range of wavelengths; thus, there is an upshift in the absorbance profile, as shown in Figure 3. This reveals that in the FSP process CH_4 creates a distribution of density-of-states at the edges of the conduction band (CB) and valence band (VB) of the STO, with a more profound effect of Axial-CH_4; i.e., see the extreme case of STO-R5.

We underline that in the case of Urbach-tails the estimation of the E_g-values should be done correctly, according to the method of Makula et al. [36]. In this method, the upshifted baseline should be taken to estimate the crossing point with the tangential-slope typically used in the Tauc analysis; see Figure 3B.

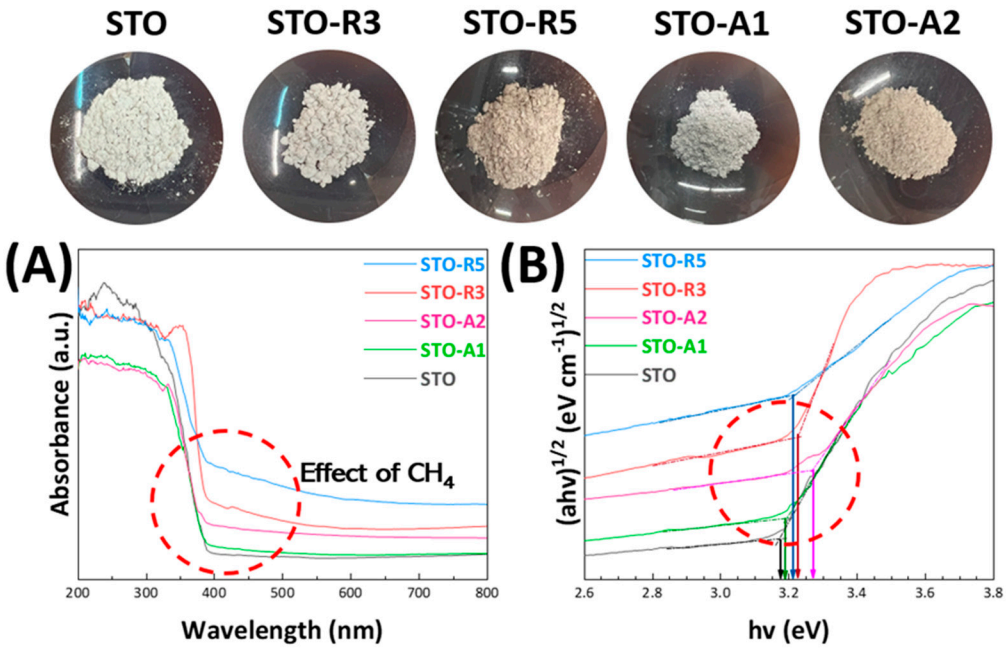

Figure 3. (**A**) UV−Vis DRS absorption spectra of STO nanomaterials. (**B**) Tauc plots with the arrows pointing at the calculated Eg values of the STO nanomaterials. (*Top Figures:* Powder nanoparticles showcasing the color change).

It is instructive to connect the effect of these Urbach-states with the drastic effect on the color of anoxic material, as shown in the photos in Figure 3 (top). The initially crisp white color of STO turned into beige-grey, without having a profound effect on the E_g values.

To get more insight into the atomic-level effect of the anoxicity on the STO-lattice, we used Raman spectroscopy to study the STO-lattice dynamics because of its sensitivity to identify short-range distortions, structural phase transitions and defects introduced in the lattice. At room temperature, STO possesses an ideal cubic perovskite structure in which first-order Raman scattering is forbidden. As Petzelt et al. [37] have reported, when symmetry is broken—either by strain engineering created from lattice mismatch or by surface reconstruction and relaxation phenomena—first-order Raman scattering can be observed. Figure 4 shows the Raman spectra for the A-FSP-made STO nanomaterials. There are two primary modes in the spectrum where TO stands for transverse optical and LO for longitudinal optical branches assigned as follows: TO_2 (182 cm^{-1}), TO_3 (257–357 cm^{-1}), LO_2 (472 cm^{-1}), TO_4 (544 cm^{-1}), broad band around 622–723 cm^{-1} and LO_4 (793 cm^{-1}). We also observe a small intensity peak at 147 cm^{-1} which corresponds to $SrCO_3$ [38] and could be formed during FSP synthesis. However, XRD data (Figure 2A) do not reveal the presence of $SrCO_3$, thus we could conclude that $SrCO_3$ is present in the materials in a small amount, possibly located on the surface. An alternative interpretation was given by Deltreggia et al., in which the peak at 149 cm^{-1} was assigned to TO_1 mode [39]. The peak at 147–149 cm^{-1} may contain contributions from to TO_1 mode of $SrTiO_3$ or the $SrCO_3$ phase, i.e., according to Deltreggia et al. However, the $SrCO_3$ phase should be strongly evidenced by a peak at 1074 cm^{-1}. This is absent in our Raman data. Thus, we exclude assignment to $SrCO_3$. The absence of this phase is also evidenced from the XRD. The above-mentioned phonon branches and their respective values are summarized in Table 3. The lowest frequency modes (LO_1) arise due to the B-ion motion against oxygen vibrations. The

intermediate frequency modes (LO_2/TO_2) emerge from A-ion vibrations and the highest frequency vibrations are due to oxygen vibrations in BO_6 octahedra in the ABO_3 lattice.

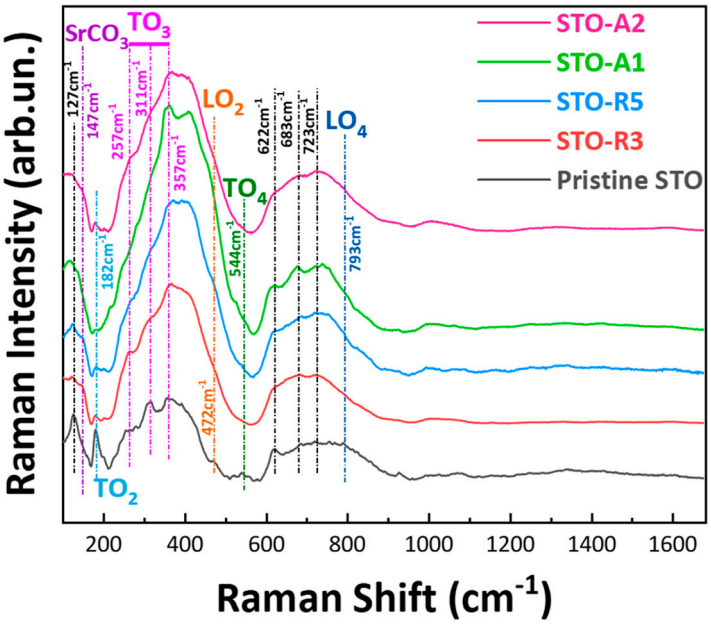

Figure 4. Raman spectra of the FSP−made STO nanomaterials, with the characteristic transverse optical band modes of TO_1, TO_2, TO_3, and TO_4 and, additionally, the characteristic longitudinal optical band modes of LO_2 and LO_4.

The presence of first-order Raman peaks at 182 cm^{-1} (O-Sr-O), 257 cm^{-1} (O-Sr-O) and 544 cm^{-1} (Ti-O-Ti) indicates that FSP-made STO perovskite is not strain-free. This is understood if we consider that FSP synthesis is accomplished in a matter of seconds. In this time window the 'A' atoms, which are usually larger than the 'B' atoms, will form a crystal. Du et al. [40] have also observed the first-order modes in polycrystalline $SrTiO_3$ even at 300 K, which is attributed to oxygen vacancies and strain effects. Moreover, the presence of dopants, e.g., such as Ca, or the application of an external electric field was found to break the symmetry of $SrTiO_3$; hence, this causes the appearance of first-order phonon modes [41,42].

Table 3. Summarized Raman band frequencies and their corresponding phonon branches of $SrTiO_3$.

Phonon Branch	Assignment	Raman Shift (cm^{-1})	Raman Shift (cm^{-1}) (Literature)
TO_1 or $SrCO_3$	Ti-O-Ti or $SrCO_3$	147	149 [38], 149 [39]
LO_1, TO_2	O-Sr-O	182	178 [38], 177 [39], 180 [43],190 [44]
TO_3, LO_3	O-Sr-O	257	271 [38], 289 [39], 274 [43], 250–348 [44]
		311	
		357	
LO_2		472	482 [39]
TO_4	Ti-O-Ti	544	543 [38], 545 [39], 546 [43], 539 [44]
		622	730 [39], (591, 655, 713) [43], 621–718 [44], (617, 667, 722) [45]
		683	
		723	
LO_4	Ti-O	793	795 [38], 795 [39], 803 [43], 786 [44]

In this context, the present Raman data reveal that the use of CH_4, either axially or radially, exerts a dramatic effect on TO_2-modes. Theoretically, a TO_2 mode is associated with vibrations of A-ion, herein the Sr, in the ABO_3 structure and a potential increase is due to distortions in the order of a wavelength in the STO lattice [46]. Moreover, TO_2 and TO_4 are polar modes while TO_3 is a non-polar mode that corresponds to the bending of the O_6 octahedra [47]; variation of the polar modes points out the polarization characteristics of STO nanoparticles (NPs). Wu et al. [45] had observed an increase in the intensity of the TO_2 mode, which was correlated with a decrease in the grain size. Thus, in the present cases the enhanced intensity of TO_2 mode implies the formation of micropolar regions in STO NPs, which can be ascribed to the enhanced surface-defect dipoles on the grain boundaries [45]. Interestingly, TO_3 mode exhibits different behavior than TO_2. Previous studies have shown that TO_3 phonon activation is associated with long-range structural distortions [48]. Therefore, the intensity increase of TO_3 mode in STO-R3, STO-R5, STO-A1 and STO-A2 is interpreted as a suppression of long-range structural distortion [40,45]. Wu et al. have observed the softening of TO_2 and TO_3 modes by decreasing the grain size of $SrTiO_3$, which suggests an increase of the Ti-O bond length. Their observation was coupled with an increase of the lattice parameter α from 3.907 Å to 3.922 Å when decreasing the size from 80 nm to 10 nm [45]. In our case, we observe a loss in the intensity of TO_2 and the softening of TO_3 modes, going from STO to the more reduced materials, i.e., STO-R5 and STO-A2. Rietveld analysis of the XRD pattern yields a cubic lattice parameter α = 3.906 Å, 3.905 Å and 3.906 Å for STO, STO-R5 and STO-A2, respectively; values that are close to that of the ideal STO (3.905 Å) [37]. Importantly, the FSP-made nano-STO's observed loss of TO_2 mode indicates an increased lattice-symmetry. This could be correlated with an increase in combustion-enthalpy, i.e., due to excess CH_4. This implies that the role of CH_4 in A-FSP technology might be more complex than simply creating a reducing environment. For FSP-made perovskites this increase in enthalpy could either affect the crystallinity of the final material or may result in materials with higher lattice symmetry. This beneficial role is evident in the Raman spectra through the loss of modes that signify a break of symmetry.

To further investigate the effect of CH_4 during the synthetic process, X-ray photoelectron spectroscopy (XPS) has been employed. Figure 5A,B present the spectra of Ti 2*p* and O 1*s*, respectively. Additional XPS data concerning the Sr 3*d* can be found in Supplementary Materials Figure S2. The primary focus is directed towards titanium and oxygen, with the aim of discerning oxygen vacancies and reduced states within the crystal structure of the five materials.

Figure 5A shows the Ti 2*p* XPS spectra, with the five materials possessing binding energies attributed to the Ti $2p_{3/2}$ and Ti $2p_{1/2}$ corroborating the oxidation state of Ti^{4+}. The pristine material has, correspondingly, 457.7 eV and 463.4 eV [49], but with increased anoxic FSP conditions a gradual higher energy shift is observed on the XPS signals of Ti 2*p* and O 1*s*. The largest energy shift of 0.9 eV occurs with the axial CH_4 conditions. The phenomenon of XPS shifting to higher binding energies has occurred with other synthesis methods, resulting in $SrTiO_3$ that have oxygen vacancies [15,17] as well as TiO_2 materials that have oxygen vacancies [50,51]. The axial or radial insertion of CH_4 induces defects in the $SrTiO_3$ crystal structure that push the Fermi level upwards by increasing the equilibrium electron density, resulting in the 0.9 eV positive shift [52,53]. Regarding the Strontium XPS data presented in Figure S2, the observed binding energies for the five materials were approximately 133.2 eV and 134.9 eV; which corresponds to Sr $3d_{5/2}$ and Sr $3d_{3/2}$, respectively. These values denote the oxidation state of Strontium as the Sr^{2+} state [13,54].

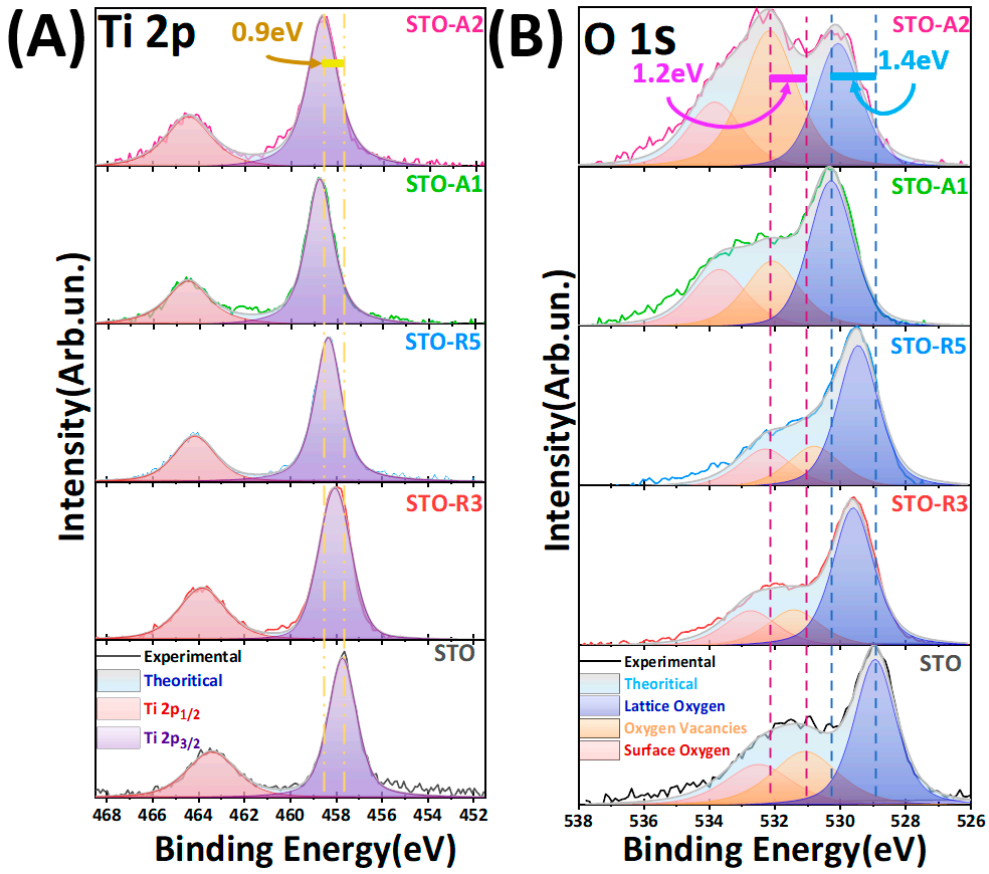

Figure 5. (**A**) XPS measurements of the five materials for the fitted Ti $2p_{1/2}$ and Ti $2p_{3/2}$ XPS spectra; (**B**) oxygen XPS measurements of the five materials for the fitted lattice oxygen, oxygen vacancies, and surface oxygen-XPS spectra.

For the O 1*s* XPS spectra, as depicted in Figure 5B, three Gaussian peaks have been carefully fitted. For the pristine $SrTiO_3$ (STO) material, a binding energy of 529 eV is identified. This corresponds to O^{2-} ions inherent in the crystal lattice structure, denoting lattice oxygen species [13,15]. At 532.5 eV, a peak is attributed to loosely bound oxygen derived from adsorbed oxygen molecules on the particle surface or hydroxyl groups [13,15]. The intermediate peak at 531.1 eV is associated with the concentration of oxygen vacancies within the structure [55,56]. As it is evident from the O 1*s* XPS in Figure 5B, even the pristine FSP-made STO has a high percentage of oxygen vacancies. The introduction and increase of the Radial-CH_4 causes a strong alteration in the oxygen vacancies population, shifting the oxygen species peaks. Unlike Radial-CH_4, the axially introduced CH_4 has a greater effect on the oxygen populations and species. The pronouncedly elevated area and intensity ratios in STO-A2 further support the abundance of inherent oxygen vacancies.

To further study the materials and their mass change (Δm), TG-DTA measurements were performed (Figure S3). Based on the XPS measurements, STO-A1 and STO-A2 have been selected due to their higher amounts of Vos. We have divided the TGA profile in two regions of interest. First, we have the low-temperature region between 25 °C and 200 °C, which corresponds to the loss of physiosorbed water from the nanoparticles [57]. Second, in the region between 200 and 550 °C, we have mass loss due to the decomposition of C-O, C-C and C-H bonds of non-graphitized carbons and residual solvents [57]. We notice that pristine STO exhibits a mass loss of 6.5%, of which 2% is due to physiosorbed water and 4.5% is due to uncombusted solvents and carbon bonds, which is typical for FSP materials. However, STO-A1 and STO-A2 have a completely different TGA profile compared to STO. Both materials have a similar behavior in which their mass change is positive, i.e., gaining weight, and reaches a maximum at 250 °C of 1% and 2% for STO-A1 and STO-A2,

respectively. Then we have a slight loss from 250 °C to 400 °C, and finally, from 400 °C to 700 °C their mass change is positive once again. Since the TGA measurements were performed under synthetic air, we can attribute this behavior of STO-A1 and STO-A2 to oxygen uptake filling the Vos that were created during A-FSP synthesis.

Regarding the FSP process, we notice that Axial-CH_4 in which less CH_4 is applied has a greater impact on oxygen vacancies formation in the materials vs. the Radial-CH_4 in which higher CH_4-flows prevail. This can be understood if we take into account that in AA-FSP the CH_4 is introduced inside the flame; thus, it affects the primary particles created in the first stages of particle formation in FSP. On the other hand, Radial-CH_4 has a more subtle effect on the final material, creating fewer oxygen vacancies since the CH_4 affects the STO particles after their formation. Overall, the present results exemplify the ability of A-FSP to control at a fine level the vacancies and lattice properties of perovskite $SrTiO_3$.

4. Conclusions

In the present work, we extend the versatility of the Anoxic-FSP synthesis to the family of $SrTiO_3$ perovskite materials. We exemplify an industrial-synthesis method that allows fine control of the lattice microstructure and vacancies. Raman spectroscopy reveals the existence of long-range structural distortions on the Ti-O bond length. Moreover, the appearance of first-order Raman scattering in the majority of the materials hints at the presence of strain effects and oxygen vacancies. These results are further supported by XPS measurements. Axial- and Radial-CH_4 induces large energy shifts, increasing the equilibrium electron density. O 1*s* XPS spectra show that Axial-CH_4 can have a greater effect on the formation of oxygen vacancies than Radial-CH_4. TGA analysis reveals that while pristine STO exhibits the expected profile for FSP-made nanoparticles, the reduced STO-A1 and STO-A2 have a totally different profile, and gain weight; this further proves the existence of Vos. The modified dispersion feed used in the case of Axial-CH_4 creates a highly reducing environment at the heart of the flame affecting the particles in the early stages of their creation. Technology-wise, the present findings could provide new insights into the large-scale synthesis of reduced perovskites from FSP technology.

Supplementary Materials: The following supporting information can be downloaded at: https://www.mdpi.com/article/10.3390/nano14040346/s1, Figure S1. (A–E) N2 absorption-desorption isotherms of Pristine-STO, STO-R3, STO-R5, STO-A1 and STO-A2 perovskites synthesized using the A-FSP process. Inset: Pore size distribution plot using the BJH method. Figure S2. (A–E) Sr 3*d* XPS spectra of the five FSP and A-FSP-made STO nanomaterials. Figure S3. TGA data of the materials Pristine STO, STO-A1 and STO-A2 under synthetic air. Vertical arrows were used to mark the estimated mass change (Δm).

Author Contributions: Conceptualization, Y.D.; methodology, A.Z. and P.P.; formal analysis, A.Z. and P.P.; investigation, A.Z. and P.P.; data curation, A.Z. and P.P.; writing—original draft preparation, A.Z.; writing—review and editing, A.Z., P.P. and Y.D.; supervision, Y.D.; funding acquisition, Y.D.; All authors have read and agreed to the published version of the manuscript.

Funding: This research was funded by the project "Advanced Nanostructured Materials for Sustainable Growth: Green Energy Production/Storage, Energy Saving and Environmental Remediation" (TAEDR-0535821) which is implemented under the action "Flagship actions in interdisciplinary scientific fields with a special focus on the productive fabric" (ID 16618), Greece 2.0—National Recovery and Resilience Fund and funded by European Union NextGenerationEU.

Data Availability Statement: Data are contained within the article and supplementary materials.

Conflicts of Interest: The authors declare no conflicts of interest.

References

1. Sun, B.; Zhou, G.; Sun, L.; Zhao, H.; Chen, Y.; Yang, F.; Zhao, Y.; Song, Q. ABO_3 Multiferroic Perovskite Materials for Memristive Memory and Neuromorphic Computing. *Nanoscale Horiz.* **2021**, *6*, 939–970. [CrossRef] [PubMed]
2. Kleemann, W.; Dec, J.; Tkach, A.; Vilarinho, P.M. $SrTiO_3$—Glimpses of an Inexhaustible Source of Novel Solid State Phenomena. *Condens. Matter* **2020**, *5*, 58. [CrossRef]

3. Maiorov, B.; Baily, S.A.; Zhou, H.; Ugurlu, O.; Kennison, J.A.; Dowden, P.C.; Holesinger, T.G.; Foltyn, S.R.; Civale, L. Synergetic Combination of Different Types of Defect to Optimize Pinning Landscape Using $BaZrO_3$-Doped $YBa_2Cu_3O_7$. *Nature Mater.* **2009**, *8*, 398–404. [CrossRef] [PubMed]
4. Jung, H.S.; Park, N.-G. Perovskite Solar Cells: From Materials to Devices. *Small* **2015**, *11*, 10–25. [CrossRef] [PubMed]
5. Irshad, M.; tul Ain, Q.; Zaman, M.; Aslam, M.Z.; Kousar, N.; Asim, M.; Rafique, M.; Siraj, K.; Tabish, A.N.; Usman, M.; et al. Photocatalysis and Perovskite Oxide-Based Materials: A Remedy for a Clean and Sustainable Future. *RSC Adv.* **2022**, *12*, 7009–7039. [CrossRef]
6. Phoon, B.L.; Lai, C.W.; Juan, J.C.; Show, P.; Chen, W. A Review of Synthesis and Morphology of $SrTiO_3$ for Energy and Other Applications. *Int. J. Energy Res.* **2019**, *43*, 5151–5174. [CrossRef]
7. Suárez-Vázquez, S.I.; Gil, S.; García-Vargas, J.M.; Cruz-López, A.; Giroir-Fendler, A. Catalytic Oxidation of Toluene by $SrTi_{1-X}B_XO_3$ (B = Cu and Mn) with Dendritic Morphology Synthesized by One Pot Hydrothermal Route. *Appl. Catal. B Environ.* **2018**, *223*, 201–208. [CrossRef]
8. Moos, R.; Hardtl, K.H. Defect Chemistry of Donor-Doped and Undoped Strontium Titanate Ceramics between 1000° and 1400 °C. *J. Am. Ceram. Soc.* **2005**, *80*, 2549–2562. [CrossRef]
9. Opoku, F.; Govender, K.K.; van Sittert, C.G.C.E.; Govender, P.P. Enhancing Charge Separation and Photocatalytic Activity of Cubic $SrTiO_3$ with Perovskite-Type Materials $MTaO_3$ (M=Na, K) for Environmental Remediation: A First-Principles Study. *ChemistrySelect* **2017**, *2*, 6304–6316. [CrossRef]
10. Zhang, C.; Jiang, N.; Xu, S.; Li, Z.; Liu, X.; Cheng, T.; Han, A.; Lv, H.; Sun, W.; Hou, Y. Towards High Visible Light Photocatalytic Activity in Rare Earth and N Co-Doped $SrTiO_3$: A First Principles Evaluation and Prediction. *RSC Adv.* **2017**, *7*, 16282–16289. [CrossRef]
11. Chen, H.-C.; Huang, C.-W.; Wu, J.C.S.; Lin, S.-T. Theoretical Investigation of the Metal-Doped $SrTiO_3$ Photocatalysts for Water Splitting. *J. Phys. Chem. C* **2012**, *116*, 7897–7903. [CrossRef]
12. Wang, J.; Wang, T.; Zhao, Z.; Wang, R.; Wang, C.; Zhou, F.; Li, S.; Zhao, L.; Feng, M. Regulation of Oxygen Vacancies in $SrTiO_3$ Perovskite for Efficient Photocatalytic Nitrogen Fixation. *J. Alloys Compd.* **2022**, *902*, 163865. [CrossRef]
13. Ura, B.; Trawczyński, J.; Kotarba, A.; Bieniasz, W.; Illán-Gómez, M.J.; Bueno-López, A.; López-Suárez, F.E. Effect of Potassium Addition on Catalytic Activity of $SrTiO_3$ Catalyst for Diesel Soot Combustion. *Appl. Catal. B Environ.* **2011**, *101*, 169–175. [CrossRef]
14. Niishiro, R.; Tanaka, S.; Kudo, A. Hydrothermal-Synthesized $SrTiO_3$ Photocatalyst Codoped with Rhodium and Antimony with Visible-Light Response for Sacrificial H_2 and O_2 Evolution and Application to Overall Water Splitting. *Appl. Catal. B Environ.* **2014**, *150–151*, 187–196. [CrossRef]
15. Tan, H.; Zhao, Z.; Zhu, W.; Coker, E.N.; Li, B.; Zheng, M.; Yu, W.; Fan, H.; Sun, Z. Oxygen Vacancy Enhanced Photocatalytic Activity of Pervoskite $SrTiO_3$. *ACS Appl. Mater. Interfaces* **2014**, *6*, 19184–19190. [CrossRef] [PubMed]
16. Deligiannakis, Y.; Mantzanis, A.; Zindrou, A.; Smykala, S.; Solakidou, M. Control of Monomeric Vo's Versus Vo Clusters in ZrO_{2-x} for Solar-Light H_2 Production from H_2O at High-Yield (Millimoles gr^{-1} h^{-1}). *Sci Rep* **2022**, *12*, 15132. [CrossRef]
17. Li, C.-Q.; Yi, S.-S.; Chen, D.; Liu, Y.; Li, Y.-J.; Lu, S.-Y.; Yue, X.-Z.; Liu, Z.-Y. Oxygen Vacancy Engineered $SrTiO_3$ Nanofibers for Enhanced Photocatalytic H_2 Production. *J. Mater. Chem. A* **2019**, *7*, 17974–17980. [CrossRef]
18. Fan, Y.; Liu, Y.; Cui, H.; Wang, W.; Shang, Q.; Shi, X.; Cui, G.; Tang, B. Photocatalytic Overall Water Splitting by $SrTiO_3$ with Surface Oxygen Vacancies. *Nanomaterials* **2020**, *10*, 2572. [CrossRef] [PubMed]
19. Qin, Y.; Fang, F.; Xie, Z.; Lin, H.; Zhang, K.; Yu, X.; Chang, K. La,Al-Codoped $SrTiO_3$ as a Photocatalyst in Overall Water Splitting: Significant Surface Engineering Effects on Defect Engineering. *ACS Catal.* **2021**, *11*, 11429–11439. [CrossRef]
20. Dimitriou, C.; Psathas, P.; Solakidou, M.; Deligiannakis, Y. Advanced Flame Spray Pyrolysis (FSP) Technologies for Engineering Multifunctional Nanostructures and Nanodevices. *Nanomaterials* **2023**, *13*, 3006. [CrossRef]
21. Psathas, P.; Solakidou, M.; Mantzanis, A.; Deligiannakis, Y. Flame Spray Pyrolysis Engineering of Nanosized Mullite-$Bi_2Fe_4O_9$ and Perovskite-$BiFeO_3$ as Highly Efficient Photocatalysts for O_2 Production from H_2O Splitting. *Energies* **2021**, *14*, 5235. [CrossRef]
22. Psathas, P.; Moularas, C.; Smykała, S.; Deligiannakis, Y. Highly Crystalline Nanosized $NaTaO_3$/NiO Heterojunctions Engineered by Double-Nozzle Flame Spray Pyrolysis for Solar-to-H_2 Conversion: Toward Industrial-Scale Synthesis. *ACS Appl. Nano Mater.* **2023**, *6*, 2658–2671. [CrossRef]
23. Yuan, X.; Meng, L.; Zheng, C.; Zhao, H. Deep Insight into the Mechanism of Catalytic Combustion of CO and CH_4 over $SrTi_{1-x}B_xO_3$ (B = Co, Fe, Mn, Ni, and Cu) Perovskite via Flame Spray Pyrolysis. *ACS Appl. Mater. Interfaces* **2021**, *13*, 52571–52587. [CrossRef] [PubMed]
24. Yuan, X.; Meng, L.; Xu, Z.; Zheng, C.; Zhao, H. CuO Quantum Dots Supported by $SrTiO_3$ Perovskite Using the Flame Spray Pyrolysis Method: Enhanced Activity and Excellent Thermal Resistance for Catalytic Combustion of CO and CH_4. *Environ. Sci. Technol.* **2021**, *55*, 14080–14086. [CrossRef] [PubMed]
25. Psathas, P.; Zindrou, A.; Papachristodoulou, C.; Boukos, N.; Deligiannakis, Y. In Tandem Control of La-Doping and CuO-Heterojunction on $SrTiO_3$ Perovskite by Double-Nozzle Flame Spray Pyrolysis: Selective H_2 vs. CH_4 Photocatalytic Production from H_2O/CH_3OH. *Nanomaterials* **2023**, *13*, 482. [CrossRef] [PubMed]
26. Zindrou, A.; Belles, L.; Solakidou, M.; Boukos, N.; Deligiannakis, Y. Non-Graphitized Carbon/Cu_2O/Cu^0 Nanohybrids with Improved Stability and Enhanced Photocatalytic H2 Production. *Sci. Rep.* **2023**, *13*, 13999. [CrossRef]

27. Fragou, F.; Zindrou, A.; Deligiannakis, Y.; Louloudi, M. Carbon–SiO_2 Hybrid Nanoparticles with Enhanced Radical Stabilization and Biocide Activity. *ACS Appl. Nano Mater.* **2023**, *6*, 20841–20854. [CrossRef]
28. Teoh, W.Y.; Amal, R.; Mädler, L. Flame Spray Pyrolysis: An Enabling Technology for Nanoparticles Design and Fabrication. *Nanoscale* **2010**, *2*, 1324. [CrossRef]
29. Zindrou, A.; Deligiannakis, Y. Quantitative In Situ Monitoring of Cu-Atom Release by Cu_2O Nanocatalysts under Photocatalytic CO_2 Reduction Conditions: New Insights into the Photocorrosion Mechanism. *Nanomaterials* **2023**, *13*, 1773. [CrossRef]
30. Patterson, A.L. The Scherrer Formula for X-Ray Particle Size Determination. *Phys. Rev.* **1939**, *56*, 978–982. [CrossRef]
31. Tauc, J.; Grigorovici, R.; Vancu, A. Optical Properties and Electronic Structure of Amorphous Germanium. *Phys. Status Solidi (B)* **1966**, *15*, 627–637. [CrossRef]
32. Brunauer, S.; Emmett, P.H.; Teller, E. Adsorption of Gases in Multimolecular Layers. *J. Am. Chem. Soc.* **1938**, *60*, 309–319. [CrossRef]
33. Koirala, R.; Pratsinis, S.E.; Baiker, A. Synthesis of Catalytic Materials in Flames: Opportunities and Challenges. *Chem. Soc. Rev.* **2016**, *45*, 3053–3068. [CrossRef]
34. Urbach, F. The Long-Wavelength Edge of Photographic Sensitivity and of the Electronic Absorption of Solids. *Phys. Rev.* **1953**, *92*, 1324. [CrossRef]
35. Aljishi, S.; Cohen, J.D.; Jin, S.; Ley, L. Band Tails in Hydrogenated Amorphous Silicon and Silicon-Germanium Alloys. *Phys. Rev. Lett.* **1990**, *64*, 2811–2814. [CrossRef] [PubMed]
36. Makuła, P.; Pacia, M.; Macyk, W. How To Correctly Determine the Band Gap Energy of Modified Semiconductor Photocatalysts Based on UV–Vis Spectra. *J. Phys. Chem. Lett.* **2018**, *9*, 6814–6817. [CrossRef] [PubMed]
37. Petzelt, J.; Ostapchuk, T.; Gregora, I.; Rychetský, I.; Hoffmann-Eifert, S.; Pronin, A.V.; Yuzyuk, Y.; Gorshunov, B.P.; Kamba, S.; Bovtun, V.; et al. Dielectric, Infrared, and Raman Response of Undoped $SrTiO_3$ Ceramics: Evidence of Polar Grain Boundaries. *Phys. Rev. B* **2001**, *64*, 184111. [CrossRef]
38. Da Silva, L.F.; Avansi, W.; Andrés, J.; Ribeiro, C.; Moreira, M.L.; Longo, E.; Mastelaro, V.R. Long-Range and Short-Range Structures of Cube-like Shape $SrTiO_3$ Powders: Microwave-Assisted Hydrothermal Synthesis and Photocatalytic Activity. *Phys. Chem. Chem. Phys.* **2013**, *15*, 12386. [CrossRef] [PubMed]
39. Deltreggia, L.A.; Bernardi, M.I.B.; Mesquita, A. Influence of La Substitution on Local Structural and Photoluminescence Properties of $SrTiO_3$:Pr Phosphor. *Scr. Mater.* **2018**, *157*, 15–18. [CrossRef]
40. Du, Y.L.; Chen, G.; Zhang, M.S. Investigation of Structural Phase Transition in Polycrystalline $SrTiO_3$ Thin Films by Raman Spectroscopy. *Solid State Commun.* **2004**, *130*, 577–580. [CrossRef]
41. Kleemann, W.; Albertini, A.; Kuss, M.; Lindner, R. Optical Detection of Symmetry Breaking on a Nanoscale in $SrTiO_3$:Ca. *Ferroelectrics* **1997**, *203*, 57–74. [CrossRef]
42. Akimov, I.A.; Sirenko, A.A.; Clark, A.M.; Hao, J.-H.; Xi, X.X. Electric-Field-Induced Soft-Mode Hardening in $SrTiO_3$ Films. *Phys. Rev. Lett.* **2000**, *84*, 4625–4628. [CrossRef] [PubMed]
43. Hadj Youssef, A.; Zhang, J.; Ehteshami, A.; Kolhatkar, G.; Dab, C.; Berthomieu, D.; Merlen, A.; Légaré, F.; Ruediger, A. Symmetry-Forbidden-Mode Detection in $SrTiO_3$ Nanoislands with Tip-Enhanced Raman Spectroscopy. *J. Phys. Chem. C* **2021**, *125*, 6200–6208. [CrossRef]
44. Gu, L.; Wei, H.; Peng, Z.; Wu, H. Defects Enhanced Photocatalytic Performances in $SrTiO_3$ Using Laser-Melting Treatment. *J. Mater. Res.* **2017**, *32*, 748–756. [CrossRef]
45. Wu, X.; Wu, D.; Liu, X. Negative Pressure Effects in $SrTiO_3$ Nanoparticles Investigated by Raman Spectroscopy. *Solid State Commun.* **2008**, *145*, 255–258. [CrossRef]
46. Moreira, M.L.; Longo, V.M.; Avansi, W., Jr.; Ferrer, M.M.; Andrés, J.; Mastelaro, V.R.; Varela, J.A.; Longo, É. Quantum Mechanics Insight into the Microwave Nucleation of $SrTiO_3$ Nanospheres. *J. Phys. Chem. C* **2012**, *116*, 24792–24808. [CrossRef]
47. Hlinka, J.; Petzelt, J.; Kamba, S.; Noujni, D.; Ostapchuk, T. Infrared Dielectric Response of Relaxor Ferroelectrics. *Phase Transit.* **2006**, *79*, 41–78. [CrossRef]
48. Toulouse, J.; DiAntonio, P.; Vugmeister, B.E.; Wang, X.M.; Knauss, L.A. Precursor Effects and Ferroelectric Macroregions in $KTa_{1-x}Nb_xO_3$ and $K_{1-y}Li_yTaO_3$. *Phys. Rev. Lett.* **1992**, *68*, 232–235. [CrossRef] [PubMed]
49. Peng, W.-C.; Chen, Y.-C.; He, J.-L.; Ou, S.-L.; Horng, R.-H.; Wuu, D.-S. Tunability of P- and n-Channel TiO_x Thin Film Transistors. *Sci. Rep.* **2018**, *8*, 9255. [CrossRef]
50. Abdullah, S.A.; Sahdan, M.Z.; Nayan, N.; Embong, Z.; Hak, C.R.C.; Adriyanto, F. Neutron Beam Interaction with Rutile TiO_2 Single Crystal (1 1 1): Raman and XPS Study on Ti^{3+}-Oxygen Vacancy Formation. *Mater. Lett.* **2020**, *263*, 127143. [CrossRef]
51. Bi, X.; Du, G.; Kalam, A.; Sun, D.; Yu, Y.; Su, Q.; Xu, B.; Al-Sehemi, A.G. Tuning Oxygen Vacancy Content in TiO_2 Nanoparticles to Enhance the Photocatalytic Performance. *Chem. Eng. Sci.* **2021**, *234*, 116440. [CrossRef]
52. Yu, W.; Ou, G.; Si, W.; Qi, L.; Wu, H. Defective $SrTiO_3$ Synthesized by Arc-Melting. *Chem. Commun.* **2015**, *51*, 15685–15688. [CrossRef]
53. Sun, T.; Lu, M. Band-Structure Modulation of $SrTiO_3$ by Hydrogenation for Enhanced Photoactivity. *Appl. Phys. A* **2012**, *108*, 171–175. [CrossRef]
54. Li, W.; Liu, S.; Wang, S.; Guo, Q.; Guo, J. The Roles of Reduced Ti Cations and Oxygen Vacancies in Water Adsorption and Dissociation on $SrTiO_3$ (110). *J. Phys. Chem. C* **2014**, *118*, 2469–2474. [CrossRef]

55. Wei, Z.; Zhao, M.; Yang, Z.; Duan, X.; Jiang, G.; Li, G.; Zhang, F.; Hao, Z. Oxygen Vacancy-Engineered Titanium-Based Perovskite for Boosting H_2O Activation and Lower-Temperature Hydrolysis of Organic Sulfur. *Proc. Natl. Acad. Sci. USA* **2023**, *120*, e2217148120. [CrossRef] [PubMed]
56. Baek, J.-Y.; Duy, L.T.; Lee, S.Y.; Seo, H. Aluminum Doping for Optimization of Ultrathin and High-k Dielectric Layer Based on $SrTiO_3$. *J. Mater. Sci. Technol.* **2020**, *42*, 28–37. [CrossRef]
57. Gomez-Martin, A.; Schnepp, Z.; Ramirez-Rico, J. Structural Evolution in Iron-Catalyzed Graphitization of Hard Carbons. *Chem. Mater.* **2021**, *33*, 3087–3097. [CrossRef]